Check for updates

Optoelectronic and solar cell applications of Janus monolayers and their van der Waals heterostructures†

M. Idrees,[a] H. U. Din,[a] R. Ali,[b] G. Rehman,[c] T. Hussain,[d] C. V. Nguyen, [ID] *[e]
Iftikhar Ahmad*[cf] and B. Amin [ID] *[f]

Janus monolayers and their van der Waals heterostuctures are investigated by hybrid density functional theory calculations. MoSSe, WSSe, MoSeTe and WSeTe are found to be direct band gap semiconductors. External electric fields are used to transform indirect MoSTe and WSTe to direct band gap semiconductors. MoSSe–WSSe, MoSeTe–WSeTe and MoSTe–WSTe vdW heterostructures are also indirect band gap semiconductors with type-II band alignment. Similar to the corresponding monolayers, in some of the above mentioned vdW heterostructures an external electric field and tensile strain can transform indirect to direct band gaps, while sustaining type-II band alignment. Janus monolayers have lower values of the work function (ϕ) than their vdW heterostructure counterparts. Furthermore, absorption spectra, absorption efficiency, and valence(conduction) band edge potentials are calculated to understand the optical and photocatalytic behavior of these systems. Red and blue shifts are observed in the position of excitonic peaks due to the induced strain in Janus monolayers. Strong device absorption efficiencies (80–90%) are observed for the WSeTe, MoSTe and WSTe monolayers in the visible, infra-red and ultraviolet regions. Energetically favourable band edge positions in Janus monolayers make them suitable for water splitting at zero pH. We find that the MoSSe–WSSe heterostructure and the MoSTe monolayer are promising candidates for water splitting with conduction and valence band edges positioned just out-side of the redox interval.

I. Introduction

The incredible thinness of graphene with exceptional semiconducting direct band gap (1.0–2.0 eV) nature, high carrier mobility (> 200 cm^2 V^{-1} s^{-1}), and high ambient stability makes MX$_2$ (M = Mo, W; X = S, Se, Te) monolayers ideal candidates for optoelectronic devices.[1–5] Recently, selenization in MoS$_2$[6] and sulfurization in MoSe$_2$[7] through chemical vapor deposition (CVD) have been confirmed successfully as Janus MXY (M = Mo, W; X, Y = S, Se, Te) monolayers. Density Functional Theory (DFT)

calculations for electronic structures and Raman vibration modes of SMoSe monolayers are also found to correlate well with experiments.[7] Furthermore, larger SOC-induced Rashba spin splitting makes these materials promising for futuristic spintronic devices.[8] Very recently, using DFT calculations Xia *et al.*[9] explored the electronic structure and photocatalytic applications of MXY (M = Mo, W; X, Y = S, Se, Te) monolayers. They showed that the atomic radius and electronegativity differences of the X and Y chalcogen elements in MXY monolayers are associated with the direct–indirect band transition and induced dipole moment.

Similar to the control of dimensionality, external electric field,[10] strain engineering,[11] and vertical stacking *via* van der Waals (vdW) interactions[12,13] are also effective approaches for manipulation of the electronic properties of materials. Layer stacking in the form of a vdW heterostructure is a practical tool to design viable electronic products, like tunneling transistors,[14] flexible optoelectronic devices[15] and bipolar transistors.[16] Type-II band alignment obtained by confining the valence band maximum (VBM) and conduction band minimum (CBM) to two different layers of vdW heterostructures is capable of modulating the inter-layer transition energy and responsible for charge separation,[17]

[a] *Department of Physics, Hazara University, Mansehra 21300, Pakistan*

[b] *The Guo China-US Photonics Laboratory, Changchun Institute of Optics, Fine Mechanics and Physics Chinese Academy of Sciences, Changchun 130033, P. R. China*

[c] *Department of Physics, University of Malakand, Chakdara, 18800, Pakistan*

[d] *School of Molecular Sciences, The University of Western Australia, Perth, WA 6009, Australia*

[e] *Institute of Research and Development, Duy Tan University, Da Nang, Vietnam. E-mail: nguyenvanchuong2@duytan.edu.vn*

[f] *Department of Physics, Abbottabad University of Science and Technology, Abbottabad 22010, Pakistan. E-mail: binukhn@gmail.com*

† Electronic supplementary information (ESI) available. See DOI: 10.1039/c9cp02648g

and hence intensively used in designing advanced optoelectronic devices.[18]

Time-dependent DFT combined with nonadiabatic molecular dynamics have been used to realize ultrafast photoinduced charge separation in the MoSSe–WS$_2$ vdW heterostructure, thus it is a promising candidate in photovoltaic and optoelectronic applications.[20] Vertical vdW and lateral heterostructures of Janus MoSSe and WSSe monolayers proposed in ref. 21 exhibit type-II band alignment. Based on DFT calculations, six Janus monolayers are found to be promising candidates for photovoltaic applications.[22]

However, despite the above results using first principles calculations, the expected properties from these systems are still under debate. Therefore, a comprehensive insight is gained into the electronic structure, effective masses, work function, and photocatalytic performance of the Janus MXY (M = Mo, W; X, Y = S, Se, Te) monolayers and their vdW heterostructures. Furthermore, optical properties in terms of the imaginary part of the dielectric function ($\varepsilon_2(\omega)$) and absorption efficiency (η) are also investigated for optoelectronic and solar cell device applications. Contrary to six possible stackings of MX$_2$ (M = Mo, W; X = S, Se) monolayers,[12] twelve possible stackings (six in each Model, Model-I and Model-II) of Janus monolayers are investigated. Experimentally achievable strain is induced in MX$_2$ monolayers while generating Janus monolayers. Therefore, the biaxial strained and electric field tunable electronic structures of the Janus monolayers and their vdW heterostructures have also been considered.

II. Computational details

We employ DFT with Grimme's empirical dispersion correction[23] in the Vienna *ab initio* simulation package (VASP).[24] A 500 eV cut-off, $6 \times 6 \times 1$ k-meshes, and a 20 Å vacuum layer along the z-axis added to interrupt the artifacts of the periodic boundary conditions, are used. Energies (forces) were converged to 10^{-4} eV (10^{-3} eV Å^{-1}) by the Perdew–Burke–Ernzerhof (PBE) functional[25] in the relaxation of the atomic positions. Commonly, the PBE functional underestimates the band gap values of semiconductors; therefore, a computationally expensive HSE06 (Heyd–Scuseria–Ernzerhof) functional[26] including the effect of spin–orbit coupling is used for electronic band structure calculations. Furthermore, an external electric field[27] and mechanical strain applied by setting the optimized lattice parameters to fixed larger/smaller values[28] and relaxing the atomic positions are used to tune the electronic properties.

A $4 \times 4 \times 1$ supercell and harmonic interatomic force constants estimated by density functional perturbation theory are used *via* Phonopy code for the phonon spectrum calculations.[29,30]

The HSE06 single particle energies and wave functions are further used to calculate the quasiparticle energies in a GW$_0$ approach and to solve the Bethe–Salpeter (Tamm–Dancoff approximation) equation[31,32] to investigate the optical absorption spectra in terms of $\varepsilon_2(\omega)$. A 420 eV cut-off, 300 of NBAND, and 10 highest(lowest) valence(conduction) bands are used for

excitonic eigenstates in these calculations. Different cutoffs are adopted due to the high computational cost of GW$_0$ calculations.

Moreover, $\varepsilon_1(\omega)$ and $\varepsilon_2(\omega)$ are used as input files for the device absorption efficiency in the COMSOL-multiphysics software, briefly described in ref. 33, 34 and see Fig. 7(a). In this simulated device, a glass layer of 100 nm, indium doped tin oxide (ITO) layer of 80 nm (as anode material), and 2D monolayer and heterostructure layer of 350 nm are used. A 10 nm thick PC60BM ((6,6)-phenyl-C61-butyric acid methyl ester) known as an electron transport layer (ETL) stacked above the 2D material layer, while a 15 nm thick PCDTBT (poly(N-9′-heptadecanyl-2,7-carbazole-*alt*-5,5-(4′,7′-di(thien-2-yl)-2′,1′,3′-benzothiadiazole))) known as a hole transport layer (HTL) was used below the 2D material, for obtaining the excited carriers. A 100 nm thick bottom layer (Ag) worked as a cathode material.

III. Results and discussion

Contrary to MX$_2$ monolayers, in Janus MXY monolayers, M (transition metal atom) is sandwiched between X and Y (two different chalcogen atoms).[35] Optimized lattice parameters and bond lengths of MXY (M = Mo, W; X, Y = S, Se, Te) monolayers presented in Table 1 are about the average value of the corresponding MX$_2$ monolayers and are in agreement with theoretical[9,36] and experimental[6] findings. In agreement with ref. 9 and 22, MoSSe, WSSe, MoSeTe and WSeTe are found to be K-point direct band gap semiconductors, while MoSTe and WSTe are indirect band gap semiconductors with the VBM located at the Γ-point and the CBM at the Γ–K-point of the Brillouin zone (BZ),

Table 1 Lattice constant (a), bond length (M–X), phonon modes (A$_1$,E), band gap ($E_{\text{g-HSE}}$, $E_{\text{g-GW0}}$), valence band splitting (Δ_{VB}), work function (ϕ), binding energy (E_a, E_b, E_c, E_d, E_e, E_f), and interlayer distances (d) for monolayer and Model-I(-II) vdW hetrostructures

Janus monolayer	MoSSe	WSSe	MoSeTe	WSeTe	MoSTe	WSTe
a (Å)	3.25	3.26	3.42	3.45	3.35	3.38
M–X (Å)	2.42	2.42	2.52	2.56	2.43	2.44
M–Y (Å)	2.53	2.54	2.55	2.72	2.71	2.72
A_1 (cm^{-1})	294	282	210	214	236	222
E (cm^{-1})	345	332	263	227	336	318
$E_{\text{g-HSE}}$ (eV)	2.24	2.16	1.84	1.70	1.52	1.50
$E_{\text{g-GW0}}$ (eV)	3.15	3.29	2.66	2.78	2.44	2.52
Δ_{VB} (eV)	0.19	0.47	0.20	0.47	0.19	0.50
ϕ (eV)	2.53	3.00	2.55	2.82	3.10	2.88

	MoSSe–WSSe		MoSeTe–WSeTe		MoSTe–WSTe	
Heterostructures	Model-I	Model-II	Model-I	Model-II	Model-I	Model-II
E_a (eV)	−0.125	−0.131	−0.193	−0.148	−1.96	−1.93
E_b (eV)	−0.148	−0.158	−0.232	−0.182	−2.05	−2.01
E_c (eV)	−0.166	−0.183	−0.265	−0.199	−2.08	−2.02
E_d (eV)	−0.169	−0.184	−0.266	−0.200	−2.06	−2.01
E_e (eV)	−0.129	−0.135	−0.199	−0.153	−2.07	−2.00
E_f (eV)	−0.179	−0.198	−0.287	−0.211	−2.07	−2.01
d_{spacing} (Å)	3.15	3.04	3.22	3.10	3.14	3.01
a (Å)	3.25		3.43		3.36	
Mo–X/Y (Å)	2.42/2.53		2.55/2.72		2.43/2.71	
W–X/Y (Å)	2.42/2.54		2.56/2.72		2.44/2.72	
$E_{\text{g-HSE}}$ (eV)	1.45	1.62	0.77	0.94	0.44	0.52
$E_{\text{g-GW0}}$ (eV)	1.68	2.08	1.24	1.23	0.86	0.93
ϕ (eV)	4.03	5.12	4.75	5.68	4.55	6.05

This journal is © the Owner Societies 2019

Phys. Chem. Chem. Phys., 2019, **21**, 18612–18621 | **18613**

see Fig. 3. Additionally, strain is a good approach to tune the band gap, therefore strain was induced in the MX_2 (M = Mo, W; X = S, Se, Te) monolayers, while generating a Janus structure alters the band gap value, *i.e.* MS$_2$(strained) > MSSe > MSe$_2$ (strained) and MSe$_2$ (strained) > MSeTe > MTe$_2$ (strained). Hence, constructing Janus MXY structures is a good strategy for the band gap modulation of MX_2 monolayers. Compressive-(tensile) strain enhances(reduces) splitting between bonding and antibonding states at the K-point, while reduces(enhances) it along the Γ–K direction, leading to fluctuation in the nature of the band gap. In the case of all Janus TMDCs monolayers, the VBM at the K-point(Γ-point) of the BZ is mainly originating from d_{xy} + $d_{x^2-y^2}$(d_{z^2}), while the CBM is due to the d_{z^2} orbital. However, the d_{yz} and d_{xz} orbitals are not involved directly in the interplay near the CBM and VBM. Applying an external electric field split the electronic levels, and hence is also a good strategy to control the electronic properties of 2D materials.[37] An electric field of 0.34(0.50) eV Å^{-1} shifts the VBM/CBM to the Γ-point of the BZ, and hence transforms MoSTe(WSTe) to a direct band gap semiconductor, see Fig. 3(g and i), while further increase in the electric field tunes these materials to metals in agreement with ref. 37 for MX_2 monolayers. Transition from indirect to direct band gap nature and from semiconductor to metallic nature with increasing electric field is due to the fact that an external electric field induces repulsion among the electronic levels leading to an upshift(downshift) of the VBM(CBM), and thus decreases the band gap at the Γ-point instead of the K-point of the BZ for MX_2 monolayers.[37]

Layer stacking can effectively modulate the electronic structure in the formation of vdW heterostructures.[38] Therefore, maximum possible stacking configurations in each MXY–WXY vdW heterostructure are fabricated by using an optimized lattice constant of Janus monolayers. In a simple TMDC monolayer, a similar chalcogen atom is attached to the transition metal atom (X–M–X); hence, there are six favourable arrangements of atoms in a heterostructure.[12,13] In the case of Janus monolayers, two different chalcogen atoms are attached to the transition metal atom (X–M–Y), so there are twelve favourable high-symmetry

stacking sequences of atoms in the formation of a Janus vdW heterostructure,[39] separated into two models. Model-I: top layer of one chalcogen atom of one monolayer touches the bottom layer of a different chalcogen atom of a second monolayer while for Model-II: the same chalcogen atoms touch both monolayers. Model-I in Fig. 1; stacking (a) the M atom of one monolayer is placed on the top of an M atom of a second monolayer, while an X(Y) atom of one monolayer is on top of the Y(X) atom of a second monolayer, stacking (b) M atom of one monolayer is placed on top of the X/Y atom of the second monolayer and *vice versa*, stacking (c) the M atom of one monolayer is placed on top of the M atom of another monolayer while the X and Y atoms of both monolayers are on the hexagonal site, stacking (d) the M atom of one monolayer is placed on the X/Y atom of a second monolayer while the other M atom and X/Y atom of a second monolayer is on the hexagonal site, stacking (e) the M atom of the second monolayer is placed on the top of the X/Y atom of first monolayer while the M atom of the first monolayer is on the hexagonal site, stacking (f) the M atoms of both monolayers are on the hexagonal site while the X/Y atoms are on top of each other. We have also relaxed all the similar configurations in Model-II as discussed.

Binding energy (E_b); $E_b = E_{heterostructure} - E_{monolayer-i} - E_{monolayer-ii}$[12] is calculated and presented in Table 1. More negative binding energy and smaller interlayer distance owing to the stronger interaction make stacking f (similar to bulk MX_2) in both models of MoSSe–WSSe and MoSeTe–WSeTe most favourable, see Table 1. These values are in the range of previous calculated values of other vdW heterostructures.[19,39,42] Similarly, a favourable stacking position is also established in the vdW heterostructures of MX_2 monolayers.[12,13] The stability of a specific model is controlled by several factors including the strength of the hybridization tailored by strain. Therefore, in contrast to MoSSe–WSSe and MoSeTe–WSeTe, stacking c is favourable for the MoSTe–WSTe vdW heterostructure, due to the large induced strain in MX_2 while generating MXY monolayers.[40]

The phonon spectrum exhibits no imaginary phonon modes, confirming the dynamical stability of all Janus MXY monolayers
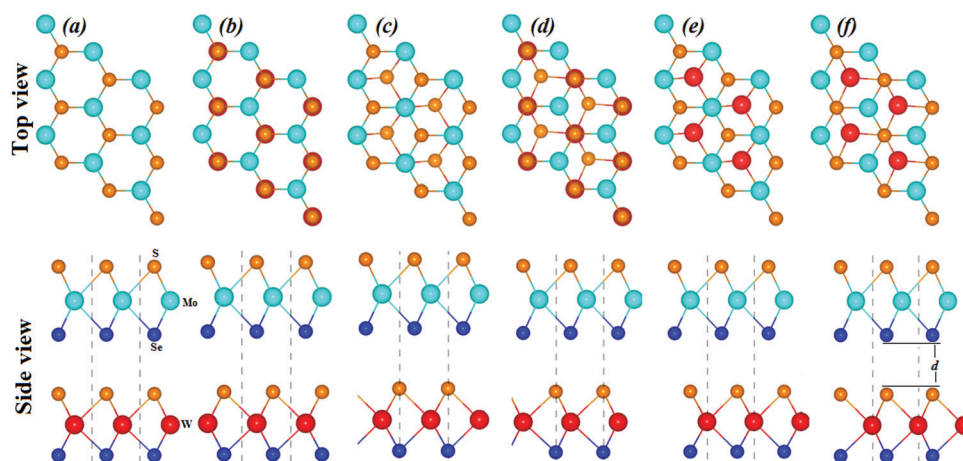

Fig. 1 Janus heterostructure in six high symmetry stacking sequences in Model-I. The dotted line represents the unit cell.
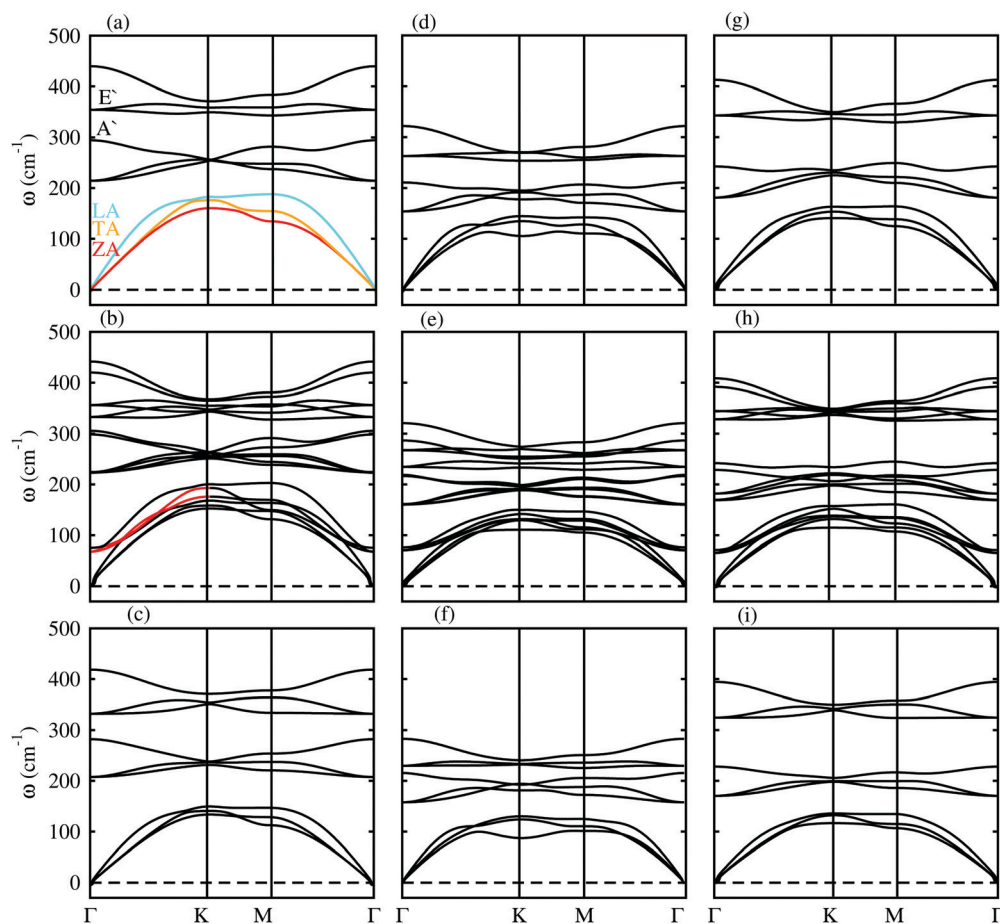
Fig. 2 Phonon spectra; (a) MoSSe, (b) MoSSe–WSSe, (c) WSSe, (d) MoSeTe, (e) MoSeTe–WSeTe, (f) WSeTe, (g) MoSTe, (h) MoSTe–WSTe, and (i) WSTe.

and their favourable vdW heterostructures, see Fig. 2. Phonon dispersion of Janus monolayers has three acoustical branches at lower frequency containing in-plane longitudinal acoustic (LA), transverse acoustic (TA), and out-of-plane acoustic (ZA) modes and six optical branches of two in-plane longitudinal optical (LO$_1$ and LO$_2$), two in-plane transverse optical (TO$_1$ and TO$_2$), and two out-of-plane optical (ZO$_1$ and ZO$_2$) modes. Six optical modes are further classified as degenerate E′ (LO$_2$ and TO$_2$) and E″ (LO$_1$ and TO$_1$) and non degenerate A1′ (ZO$_1$) and A1″ (ZO$_2$) at the Γ-point of the BZ. Vibration frequencies of A1 and E modes for the MXY monolayers in Fig. 2 are summarized in Table 1, which are in agreement with the Raman peaks at 287 and 355 cm^{-1} for MoSSe in ref. 6 and 7.

Heterostructures contain six atoms with the corresponding three acoustic and fifteen optical branches. Acoustic branches at lower frequency also hold LA, TA, and ZA modes. Apparently in all heterostructure systems (see Fig. 2) at the Γ-point, the two lowest optical modes (red color) above the acoustic mode located in the frequency range 40–60 cm^{-1}, are responsible for the vdW interaction or coupling effect between the corresponding monolayers. A similar trend has been experimentally reported in fabricating MoS$_2$–WSe$_2$ and MoSe$_2$–MoS$_2$ heterostructures[41] and theoretically predicted in SiC-TMDC heterostructures.[42]

In both Model-I and -II of MoSSe–WSSe and MoSTe–WSTe (MoSeTe–WSeTe), the VBM lies at the $\Gamma(K)$-point while the CBM lies at the Γ–K-point of the BZ; hence, they are indirect band gap semiconductors, see Fig. 3, while the band gap values are presented in Table 1. Our calculated band gap value for an untwisted bilayer (MoSSe–WSSe) is slightly larger than the values calculated in ref. 43, because we have used the HSE06 functional, while the VBM and CBM lie at the same points in the Brillouin zone. Tensile strain of 2% shifts the CBM from Γ to K-point of the BZ uniquely in MoSeTe–WSeTe (Model-I), and hence it transforms to a direct band gap semiconductor. Similar to Janus monolayers, external electric field of 0.4 eV Å^{-1} transforms indirect MoSSe–WSSe and MoSeTe–WSeTe to direct band gap semiconducting materials (see Fig. S2 in the ESI† for details). A substantial amount of induced strain maintains the indirect band gap nature of an MoSTe–WSTe semiconductor under both applied external electric field and tensile strain.

The weighted band structure of both modeled heterostructures without and with applying external electric field are investigated and presented in Fig. 4. Model-I, the VBM of MoSSe–WSSe (MoSeTe–WSeTe) heterostructures is due to the Mo-d$_{z^2}$(W-d$_{z^2}$) orbitals, while the CBM is due to the W-d$_{xy}$(Mo-d$_{xy}$) orbitals, see Fig. 4 (top row). External electric field not only transforms indirect MoSSe–WSSe and MoSeTe–WSeTe to direct

This journal is © the Owner Societies 2019

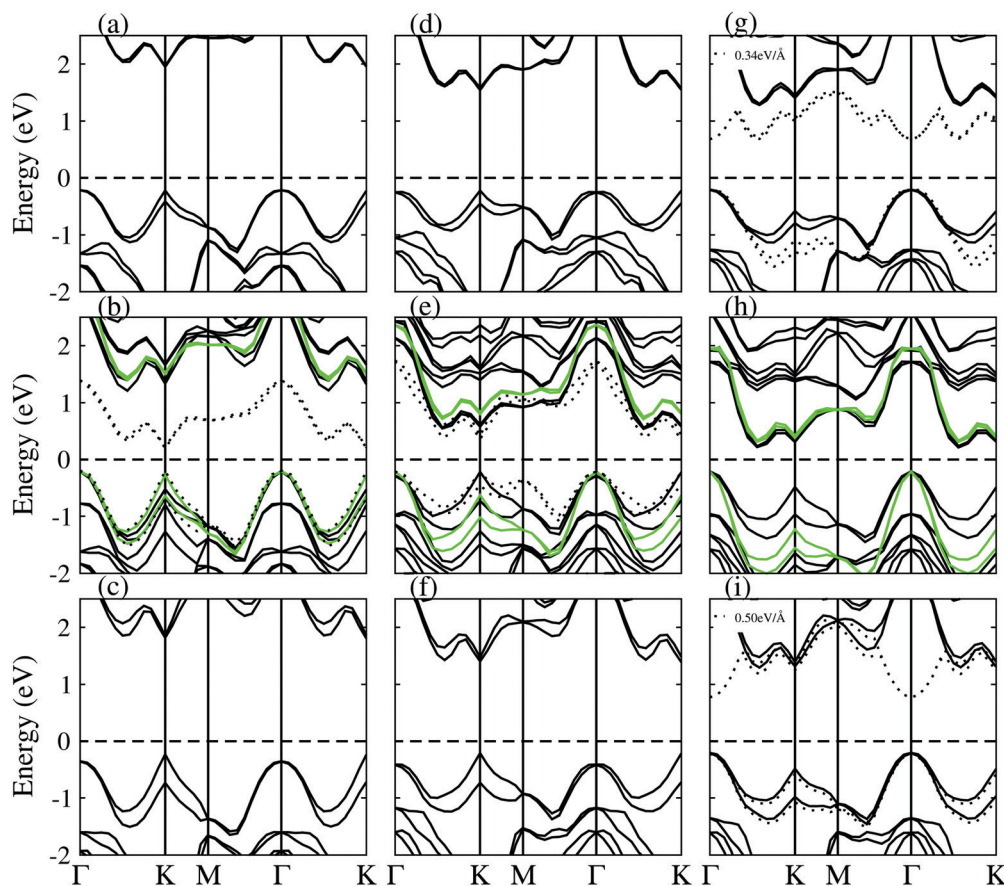*Phys. Chem. Chem. Phys.*, 2019, **21**, 18612–18621 | **18615**

Fig. 3 Band structure; (a) MoSSe, (b) MoSSe–WSSe, (c) WSSe, (d) MoSeTe, (e) MoSeTe–WSeTe, (f) WSeTe, (g) MoSTe, (h) MoSTe–WSTe, and (i) WSTe. Black color for Model-I, green color for Model-II heterostructures in (b), (e) and (h) and dotted line represents transition to direct band gap nature under the influence of electric field.

band gap semiconducting materials, but also tunes the band alignment, see Fig. 4(b and e), where the VBM of MoSSe–WSSe (MoSeTe–WSeTe) heterostructures is due to the W-d_{xy}(Mo-d_{xy}) orbital and the CBM is due to the Mo-d_{z^2}(W-d_{z^2}) orbitals. This type of VBM and CBM, separated into different layers of both modeled heterostructures, called type-II band alignment, and will spontaneously separate the free electrons and holes, and enable efficient optoelectronics and solar energy conversion applications in photovoltaics.[21] A similar trend of both electron and holes contributed by different layers is also observed in MoSTe–WSTe (Model-I, II) heterostructures, see Fig. 5. Although, in our previous work we have shown type-II band alignment for indirect band gap heterostructures, while Terrones and his co-workers[44] show the same property in direct band gap semiconducting heterostructures of MX$_2$ monolayers. In the present work, type-II band alignment is confirmed for both direct (under external electric field) and indirect (without external electric field) semiconducting band gap heterostructures.

Interlayer charge transfer tunes the electronic band structure and absorption spectra of a heterostructure with respect to the corresponding parent monolayers. Therefore, interlayer charge transfer is investigated by Bader population analysis and charge density difference $\rho = \rho_{(H)} - \rho_{(JTMDCs\text{-}i)} - \rho_{(JTMDCs\text{-}ii)}$, presented in Fig. 5(c and d), where $\rho_{(H)}$ is the charge density of the heterostructure and $\rho_{(JTMDCs\text{-}i)}$ and $\rho_{(JTMDCs\text{-}ii)}$ are the charge

densities of isolated Janus monolayers, respectively. Bader population analysis and charge density difference show the interlayer charge transition. The majority of charge is transferred from the monolayer of WSSe(MoSSe) to MoSSe(WSSe) at the interface of the Model-I(-II) MoSSe–WSSe heterostructure, see Table 2, which is also confirmed from the weighted band structure of the MoSSe–WSSe heterostructure presented in Fig. 5. Therefore stacking in Model-I(-II) turns WSSe(MoSSe) into a p-doped semiconductor, while MoSSe(WSSe) into an n-doped semiconductor. In the case of MoSeTe–WSeTe(MoSTe–WSTe) heterostructures, charges are transferred from the monolayer of MoSeTe(MoSTe) to WSeTe(WSTe) at the interface in Model-I(-II), see Table 2. Thus, MoSeTe(MoSTe) turns into p-doped, while WSeTe(WSTe) turns into an n-doped semiconductor after stacking in both Model-I(-II), hence also confirming type-II band alignment, which slows down charge recombination and is highly desirable for light harvesting applications.

Formation of the Janus monolayers and their vdW heterostructures not only modulates the band structure, but also tailors the effective masses. Therefore, effective mass of carriers for Janus monolayers and the corresponding heterostructure in both Model-I and -II are calculated by using the deformation potential theory $m^* = \hbar^2(\partial^2 E(k)/\partial k^2)^{-1}$ and band fitting to a parabola,[45] see Table 3. Induced strain in MX$_2$ (M = Mo, W; X = S, Se, Te) monolayers while generating a Janus structure alters the band gap
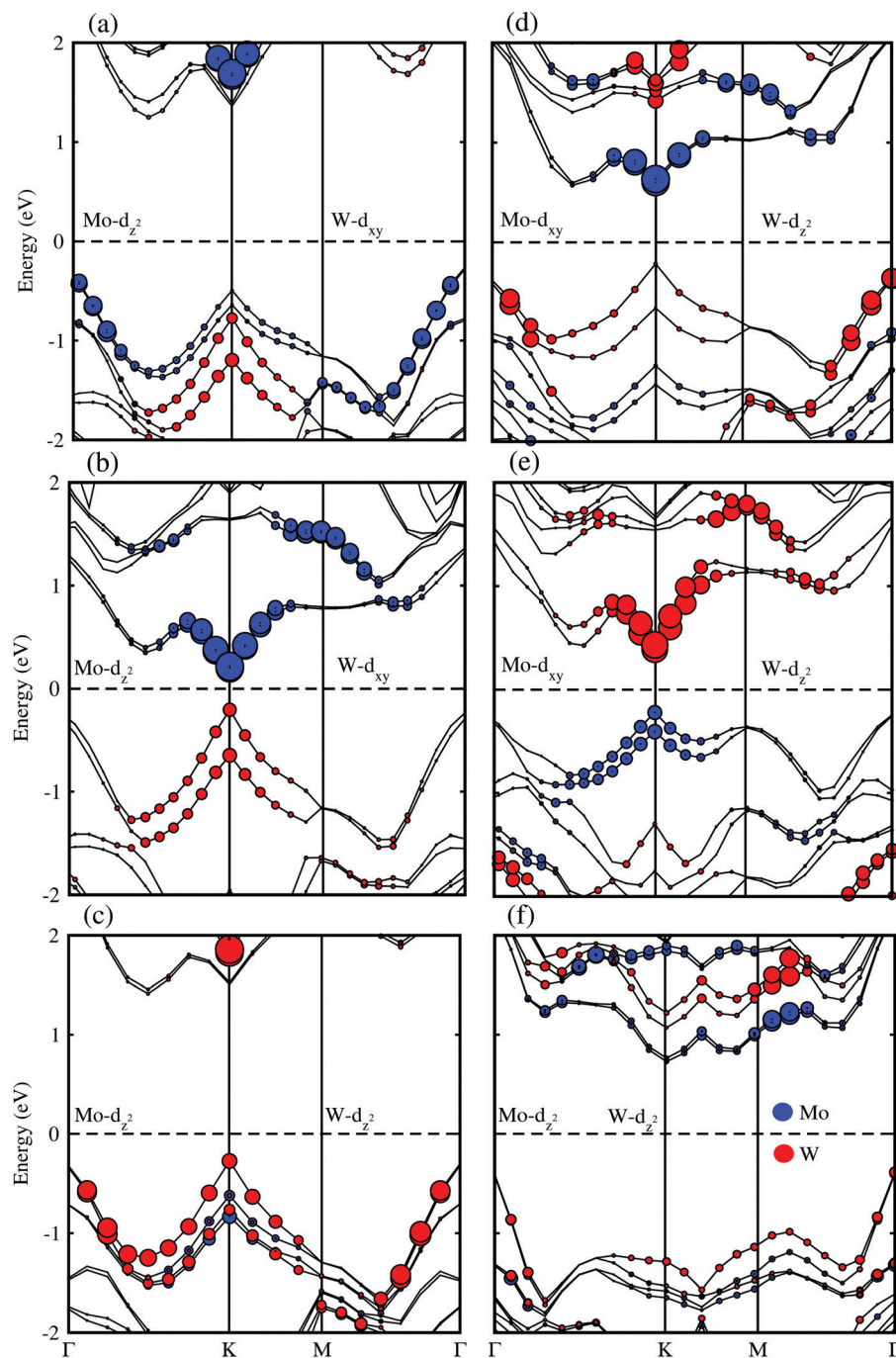
Fig. 4 Weighted band structure; MoSSe−WSSe: (a) Model-I, (b) electric field tuned Model-I, (c) Model-II; MoSeTe−WSeTe: (d) Model-I, (e) electric field tuned Model-I, (f) Model-II.

value, and hence the effective masses. Therefore, electron–hole effective masses ($m*$) of the Janus MXY monolayers are about the average value of the corresponding strained MX_2 monolayers and are in good agreement with reported[46] values. A smaller effective mass leads to higher carrier mobility, which is strongly desired for high performance device applications;[47] therefore, WSSe and WSeTe are expected as the best candidates for electronic and opto-electronic devices. It is also clear from Table 3 that the effective masses for holes and electrons of a heterostructure in

Model-I are smaller than that of Model-II, and hence shows the best candidate for electronic and opto-electronic devices. Smaller effective mass of electrons than holes for all Janus MXY monolayers and the corresponding heterostructures in both Model-I and -II are in good agreement with previous calculated results.[48]

Absorption spectra in terms of the $\varepsilon_2(\omega)$ of the Janus monolayers and their vdW heterostructures, are presented in Fig. 6. The A and B-excitons are the lowest energy transitions with the peak values at 2.0–2.2 eV for MoSSe, 2.24–2.64 eV for WSSe,
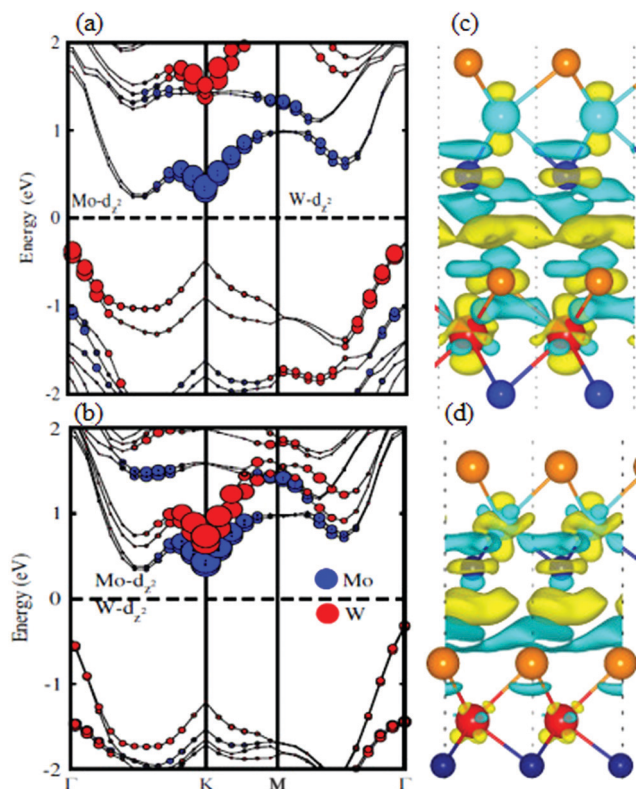
This journal is © the Owner Societies 2019

Phys. Chem. Chem. Phys., 2019, **21**, 18612–18621 | **18617**

Fig. 5 Weighted band structure; MoSTe–WSTe (a) Model-I, (b) Model-II, charge difference of the MoSSe–WSSe (c), and MoSTe–WSTe (d). The isovalue chosen to plot the isosurface is 0.001 eV Å^{-3}.

Table 3 Carrier effective masses (m^*) for electrons (m_e^*) and holes (m_h^*) of Janus monolayers and their heterostructures

Janus monolayers	MoSSe	WSSe	MoSeTe	WSeTe	MoSTe	WSTe
m_e^*	0.54	0.36	0.57	0.36	0.46	0.45
m_h^*	0.64	0.50	0.70	0.49	1.56	1.44

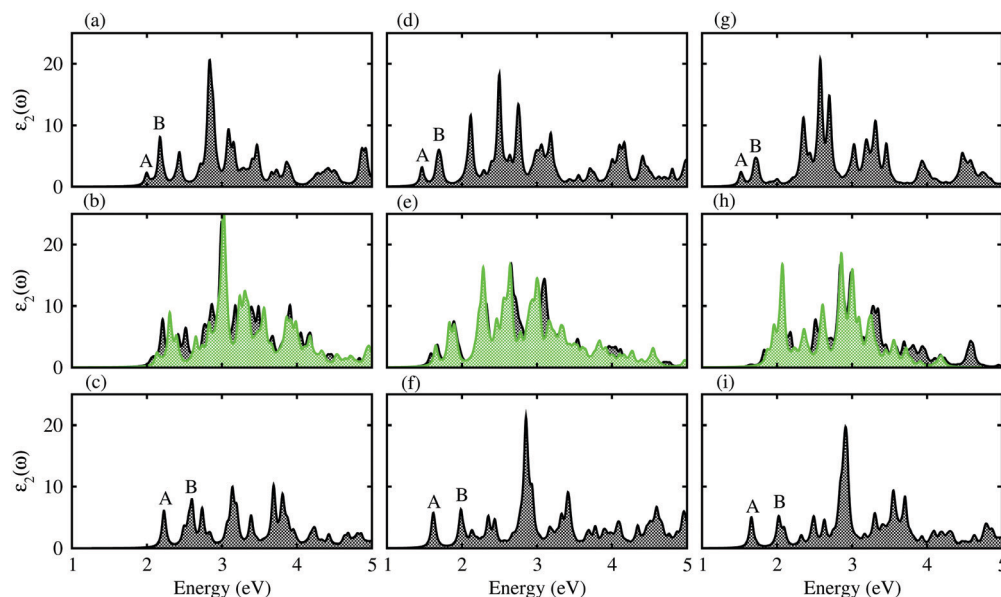|	MoSSe–WSSe		MoSeTe–WSeTe		MoSTe–WSTe	
Heterostructures	Model-I	Model-II	Model-I	Model-II	Model-I	Model-II
m_e^*	0.62	0.64	0.62	0.67	0.54	0.59
m_h^*	0.71	0.75	0.82	0.91	1.88	1.92

the position of the exciton with respect to the corresponding parent monolayers is due to charge transfer between the layers of heterostructures. This type of electron–hole separation represses the intralayer optical recombination processes.

Device absorption efficiencies are calculated to see the suitability of these materials for solar cell applications, see Fig. 7. MoSSe and WSSe show high absorption (above 60%) in the wavelength range below 700 nm and 600 nm respectively, while abrupt decrease in the absorption is found above 600 nm. MoSeTe has smaller absorption efficiency below 600 nm, while WSeTe and WSTe have excellent absorption efficiency 80–90% in a wide range of light spectra (above 800 nm). Outstanding absorption efficiency of about 90% in the spectral range of ∼840 nm is found for the MoSTe monolayer. By simulating the absorption efficiency of the corresponding heterostructures in Fig. 7, we show that there is no significant amplification in the case of all heterostructures. In the case of MoSSe–WSSe and MoSTe–WSTe, the absorption efficiency decreases in both Model-I and -II compared to their monolayer counterparts. MoSeTe–WSeTe shows higher absorption efficiency than MoSTe, while less than a WSeTe monolayer. On the basis of the above discussion, WSeTe, MoSTe and WSTe show excellent absorption efficiencies (80–90%) in a wide range of light spectra, covering the visible, infra-red and ultraviolet regions of light. It is also noted that 98% of the solar energy/photons reaching the earth's surface are below 3.4 eV, ref. 33 and 34. We can see that most of our studied materials have strong absorption efficiencies below 3.4 eV. On the basis of these findings we expect very strong power conversion efficiencies (PCE) for these 2D materials. We expect potential applications of these 2D materials in the photovoltaic industry. Therefore, we are highly encouraging experimentalists to further investigate these materials for solar cell applications.

1.48–1.65 eV for MoSeTe, 1.65–2.2 eV for WSeTe, 1.51–1.73 eV for MoSTe, and 1.67–2.02 eV for WSTe and the binding energy is 1.15 eV (MoSSe), 1.05 eV (WSSe), 1.18 eV (MoSeTe), 1.13 eV (WSeTe), 0.79 eV (MoSTe), and 1.01 eV (WSTe). Blue shift in the excitonic peaks and larger binding energy with respect to the parent monolayers in ref. 12 and 49 is due to the induced strain while constructing a Janus structure. Therefore, we have also calculated the $\varepsilon_2(\omega)$, of parent (MoS$_2$, WS$_2$, MoSe$_2$, WSe$_2$) strained monolayers, indicating that the absorption spectra can be modulated by forming Janus MXY structures. The positions of the excitonic peaks are further modulated in the heterostructures of the Janus monolayers and appear in Model-I(II) at 2.21(2.31) and 2.42(2.39) eV for MoSSe–WSSe, at 1.57(1.65) and 1.66(1.83) eV for MoSeTe–WSeTe, and at 1.83(1.88) and 2.03(2.07) eV for MoSTe–WSTe heterostructures. Hence, the above alteration in

Table 2 Bader charge ($10^{-2}\ e$) distribution in the Janus vdW heterostructures

	MoSSe–WSSe		MoSeTe–WSeTe		MoSTe–WSTe	
Heterostructures	Model-I	Model-II	Model-I	Model-II	Model-I	Model-II
Mo	0.10	0.06	0.14	0.11	0.63	0.25
W	0.10	0.12	0.13	0.12	0.53	0.30
S$_1$	0.19	−0.16	—	—	2.53	4.75
S$_2$	0.68	−0.19	—	—	0.30	−5.95
Se$_1$	−0.81	1.21	1.71	0.80	—	—
Se$_2$	−0.27	−1.03	0.22	−1.37	—	—
Te$_1$	—	—	−0.29	0.17	−0.55	0.40
Te$_2$	—	—	−1.92	0.16	−3.45	0.26
MXY/WXY	−0.52/0.51	1.11/−1.10	1.56/−1.57	1.08/−1.09	2.61/−2.62	5.40/−5.39

Fig. 6 Imaginary part of the dielectric function; (a) MoSSe, (b) MoSSe–WSSe, (c) WSSe, (d) MoSeTe, (e) MoSeTe–WSeTe, (f) WSeTe, (g) MoSTe, (h) MoSTe–WSTe, and (i) WSTe. The black color for Model-I, and green color for Model-II heterostructures in (b), (e) and (h); see the text for details.
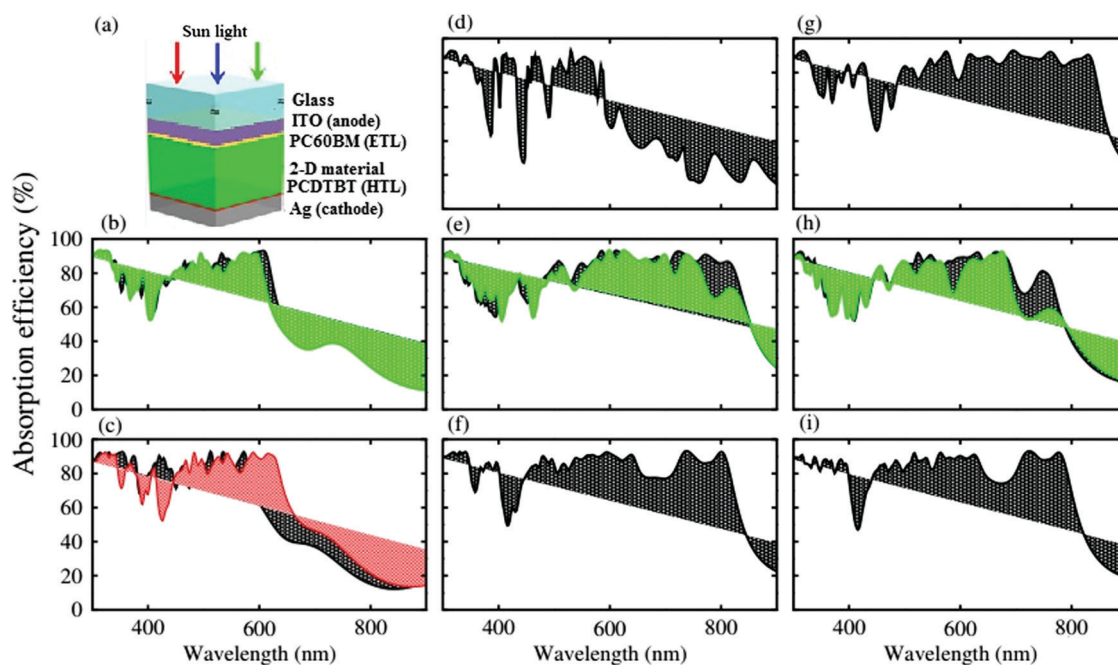
Fig. 7 (a) A simulated solar cell device structure and total device absorption efficiencies; (b) MoSSe–WSSe, (c) WSSe (black), MoSSe (red), (d) MoSeTe, (e) MoSeTe–WSeTe, (f) WSeTe, (g) MoSTe, (h) MoSTe–WSTe, and (i) WSTe. The black color for Model-I, and green color for Model-II heterostructures in (b), (e) and (h); see the text for details.

The work function (ϕ) can be defined as the minimum amount of energy needed for removing an electron from a surface. The change in conductivity of a surface, especially a monolayer, is closely related to the variation in ϕ.[50] Accurate calculation of ϕ can also help to establish the direction of charge flow in the surface. Conventionally, using DFT methods, the following relation could be used to calculate ϕ:[51] $\phi = V_\infty - E_F$, where V_∞ is the electronic potential at a vacuum region far from the surface (see Fig. SI in the ESI†) and E_F is the Fermi level. The values of ϕ for the Janus monolayers and their vdW heterostructures are given in Table 1. A comparative analysis of calculated ϕ of monolayers shows the trend, MoSTe > WSSe > WSTe > WSeTe > MoSeTe > MoSSe. For the heterostructures, we obtain the following trend MoSTe–WSTe > MoSeTe–WSeTe > MoSSe–WSSe. Thus, it can be seen that the Janus monolayers have lower values of ϕ than their heterostructure counterparts.

This journal is © the Owner Societies 2019

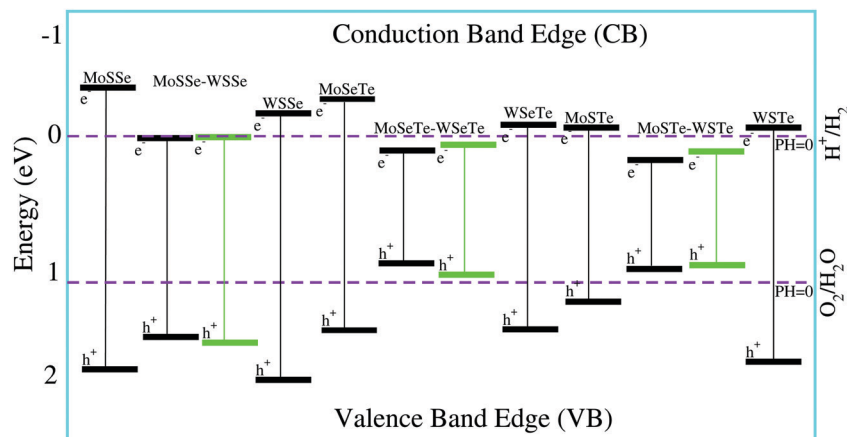Phys. Chem. Chem. Phys., 2019, 21, 18612–18621 | 18619

Fig. 8 Valence and conduction band edge potentials of Janus monolayers and their Model-I (black) and Model-II (green) vdW heterostructures. Water reduction (H^+/H_2) and oxidation (H_2O/O_2) potentials are represented by dashed lines.

TMDC monolayers, already found as low-cost and earth-abundant catalysts, can replace noble metals.[52] Therefore, the photocatalytic response of Janus monolayers and their vdW heterostructures are investigated by using Mulliken electronegativity in $E_{VBM} = \chi - E_{elec} + 0.5E_g$ and $E_{CBM} = E_{VBM} - E_g$.[53,54] Where $E_{VBM}(E_{CBM})$ is valence(conduction) band edge potential, χ represents geometric mean of Mulliken electronegativities of the constituent atoms, $E_{elec} = -4.5$ eV is the standard electrode potential on the hydrogen scale, and E_g is the band gap values. Band alignments with respect to the redox potential of water at pH = 0 for Janus monolayers and their vdW heterostructures are presented in Fig. 8. We note that our predicted band edges for the MoSSe monolayer are in good agreement with previous work (CBM: -4.88 eV, VBM: -3.80 eV).[9] Of the Janus monolayers, MoSTe exhibits the most energetically suitable positions of the band edges and hence is a promising candidate for water splitting at pH = 0. However, it should be pointed out that all the Janus monolayers show energetically suitable positions of the band edges which are outside of the reduction and oxidation potentials (Fig. 8). Of the heterostructures, MoSSe–WSSe emerges as a good candidate for water splitting, however, all other vdW heterostructures at pH = 0 fail to reduce H^+ to H_2. We have used the Nernst equation[55,56] to investigate the water redox potentials (H^+/H_2 and H_2O/O_2) at pH = 1–7 of Janus monolayers and their corresponding heterostructures (see Table SI and SII in the ESI†). The calculated values show that by increasing the value of pH, the materials tend to be favorable for reduction while the value of oxidation further decreases.

IV. Conclusions

In summary, the vibrational properties, electronic structure, effective masses, device absorption efficiency, workfunction, optical and photocatalytic response of Janus monolayers and their vdW heterostructures were investigated using first-principles (hybrid DFT) calculations. The phonon spectrum confirms the dynamical stability of Janus monolayers and their vdW heterostructures. Pristine MoSSe, WSSe, MoSeTe and WSeTe are found to be direct band gap semiconductors, while external electric fields can transform

indirect MoSTe and WSTe to direct band gap semiconductors. MoSSe–WSSe, MoSeTe–WSeTe and MoSTe–WSTe are indirect band gap type-II semiconductors, while external electric field and tensile strain can be used in specific cases to transform them to a direct band gap semiconductor with type-II band alignment. Strong optical absorption is speculated in the visible to ultraviolet regions of these heterostructures and monolayers calculated via $\varepsilon_2(\omega)$. Monolayers of WSeTe, MoSTe and WSTe show excellent absorption efficiencies (80–90%) in the visible, infra-red and ultraviolet regions. We expect potential applications of these monolayer materials for solar cells applications in the photovoltaic industry. Janus monolayers have shown lower values of ϕ than their vdW heterostructure counterparts. All Janus monolayers are found to be favorable for water splitting at pH = 0, with MoSTe being a particularly attractive candidate with conduction and valence band edges positioned just outside of the redox interval. Of the heterostructures, MoSSe–WSSe is found to be a promising candidate for water splitting.

Conflicts of interest

There are no conflicts to declare.

References

1 G. Rehman, S. A. Khan, B. Amin, I. Ahmad, L.-Y. Gan and M. Maqbool, *J. Mater. Chem. C*, 2018, **6**, 2830.
2 Y. Xie, B. Zhang, S. Wang, D. Wang, A. Wang, Z. Wang, H. Yu, H. Zhang, Y. Chen, M. Zhao, B. Huang, L. Mei and J. Wang, *Adv. Mater.*, 2017, **29**, 1605972.
3 A. Kuc and T. Heine, *Chem. Soc. Rev.*, 2015, **44**, 2603.

4 X. Zhang, X.-F. Qiao, W. Shi, J.-B. Wu, D.-S. Jiang and P.-H. Tan, *Chem. Soc. Rev.*, 2015, **44**, 2757.

5 Z. Yin, H. Li, H. Li, L. Jiang, Y. Shi, Y. Sun, G. Lu, Q. Zhang, X. Chen and H. Zhang, *ACS Nano*, 2012, **6**, 74.

6 A.-Y. Lu, H. Zhu, J. Xiao, C.-P. Chuu, Y. Han, M.-H. Chiu, C.-C. Cheng, C.-W. Yang, K.-H. Wei, Y. Yang, Y. Wang, D. Sokaras, D. Nordlund, P. Yang, D. A. Muller, M.-Y. Chou, X. Zhang and L.-J. Li, *Nat. Nanotechnol.*, 2017, **12**, 744.

7 J. Zhang, S. Jia, I. Kholmanov, L. Dong, D. Er, W. Chen, H. Guo, Z. Jin, V. B. Shenoy, L. Shi and J. Lou, *ACS Nano*, 2017, **11**, 8192.

8 Q.-F. Yao, J. Cai, W.-Y. Tong, S.-J. Gong, J.-Q. Wang, X. Wan, C.-G. Duan and J. H. Chu, *Phys. Rev. B*, 2017, **95**, 165401.

9 C. Xia, W. Xiong, J. Du, T. Wang, Y. Peng and J. Li, *Phys. Rev. B*, 2018, **98**, 165424.

10 J. Shang, S. Zhang, X. Cheng, Z. Wei and J. Li, *RSC Adv.*, 2017, **7**, 14625.

11 S. A. Khan, B. Amin, L.-Y. Gan and I. Ahmad, *Phys. Chem. Chem. Phys.*, 2017, **19**, 14738.

12 B. Amin, N. Singh and U. Schwingenschlogl, *Phys. Rev. B: Condens. Matter Mater. Phys.*, 2015, **92**, 075439.

13 B. Amin, T. P. Kaloni, G. Schreckenbach and M. S. Freund, *Appl. Phys. Lett.*, 2016, **108**, 063105.

14 T. Roy, M. Tosun, X. Cao, H. Fang, D. H. Lien, P. Zhao, Y. Z. Chen, Y. L. Chueh, J. Guo and A. Javey, *ACS Nano*, 2015, **9**, 207.

15 O. L. Sanchez, E. A. Llad, V. Koman, A. F. Morral, A. Radenovic and A. Kis, *ACS Nano*, 2014, **8**, 3042.

16 Z. Yu, Y. Pan, Y. Shen, Z. Wang, Z.-Y. Ong, T. Xu, R. Xin, L. Pan, B. Wang, L. Sun, J. Wang, G. Zhang, Y. W. Zhang, Y. Shi and X. Wang, *Nat. Commun.*, 2014, **5**, 5290.

17 P. Rivera, J. R. Schaibley, A. M. Jones, J. S. Ross, S. F. Wu, G. Aivazian, P. Klement, K. Seyler, G. Clark, N. J. Ghimire, J. Q. Yan, D. G. Mandrus, W. Yao and X. Xu, *Nat. Commun.*, 2015, **6**, 6242.

18 X. P. Hong, J. Kim, S. F. Shi, Y. Zhang, C. H. Jin, Y. H. Sun, S. Tongay, J. Q. Wu, Y. F. Zhang and F. Wang, *Nat. Nanotechnol.*, 2014, **9**, 682.

19 M. Idrees, H. U. Din, S. A. Khan, I. Ahmad, L.-Y. Gan, C. V. Nguyen and B. Amin, *J. Appl. Phys.*, 2019, **125**, 094301.

20 Y. Liang, J. Li, H. Jin, B. Huang and Y. Dai, *J. Phys. Chem. Lett.*, 2018, **9**, 2797.

21 F. Li, W. Wei, P. Zhao, B. Huang and Y. Dai, *J. Phys. Chem. Lett.*, 2017, **8**, 5959.

22 J. Wang, H. Shu, T. Zhao, P. Liang, N. Wang, D. Cao and X. Chen, *Phys. Chem. Chem. Phys.*, 2018, **20**, 18571.

23 S. Grimme, *J. Comput. Chem.*, 2006, **27**, 1787.

24 G. Kresse and J. Furthmüller, *Phys. Rev. B: Condens. Matter Mater. Phys.*, 1996, **54**, 11169.

25 J. P. Perdew, K. Burke and M. Ernzerhof, *Phys. Rev. Lett.*, 1996, **77**, 3865.

26 J. Heyd, G. E. Scuseria and M. Ernzerhof, *J. Chem. Phys.*, 2006, **124**, 219906.

27 P. T. T. Le, N. N. Hieu, L. M. Bui, H. V. Phuc, B. D. Hoi, B. Amin and C. V. Nguyen, *Phys. Chem. Chem. Phys.*, 2018, **20**, 27856.

28 B. Amin, T. P. Kaloni, G. Schreckenbach and M. S. Freund, *RSC Adv.*, 2014, **4**, 34561.

29 S. Baroni, S. de Gironcoli, A. Dal Corso and P. Giannozzi, *Rev. Mod. Phys.*, 2001, **73**, 515.

30 A. Togo, F. Oba and I. Tanaka, *Phys. Rev. B: Condens. Matter Mater. Phys.*, 2008, **78**, 134106.

31 M. Shishkin and G. Kresse, *Phys. Rev. B: Condens. Matter Mater. Phys.*, 2006, **74**, 035101.

32 M. Rohlfing and S. G. Louie, *Phys. Rev. Lett.*, 1998, **81**, 2312.

33 R. Ali, G. J. Hou, Z. G. Zhu, Q. B. Yan, Q. R. Zheng and G. Su, *Chem. Mater.*, 2018, **30**, 718.

34 R. Ali, G. J. Hou, Z. G. Zhu, Q. B. Yan, Q. R. Zheng and G. Su, *J. Mater. Chem. A*, 2018, **6**, 9220.

35 Q.-L. Xiong, J. Zhou, J. Zhang, T. Kitamurad and Z.-H. Li, *Phys. Chem. Chem. Phys.*, 2018, **20**, 20988.

36 K. D. Pham, N. N. Hieu, H. V. Phuc, B. D. Hoi, V. V. Ilysov, B. Amin and C. V. Nguyenh, *Comput. Mater. Sci.*, 2018, **153**, 438.

37 A. Ramasubramaniam, D. Naveh and E. Towe, *Phys. Rev. B: Condens. Matter Mater. Phys.*, 2011, **84**, 205325.

38 L. Qihang, L. Li, Y. Li, Z. Gao, Z. Chen and J. Lu, *J. Phys. Chem. C*, 2012, **116**, 21556.

39 L. Yan, L. Jianwei, J. Hao, H. Baibiao and D. Ying, *J. Phys. Chem. Lett.*, 2018, **9**, 2797.

40 H. Kumar, L. Dong and V. B. Shenoy, *Sci. Rep.*, 2016, **6**, 21516.

41 C. H. Lui, Z. Ye, C. Ji, K. C. Chiu, C. T. Chou, T. I. Andersen, C. Means-Shively, H. Anderson, J. M. Wu, T. Kidd, Y. H. Lee and R. He, *Phys. Rev. B: Condens. Matter Mater. Phys.*, 2015, **91**, 165403.

42 H. U. Din, M. Idrees, G. Rehman, C. V. Nguyen, I. Ahmad, M. Maqbool and B. Amin, *Phys. Chem. Chem. Phys.*, 2018, **20**, 24168.

43 C. Long, Y. Dai, Z.-R. Gong and H. Jin, *Phys. Rev. B*, 2019, **99**, 115316.

44 H. Terrones, F. Lopez-Urias and M. Terrones, *Sci. Rep.*, 2013, **3**, 1549.

45 W. D. Lucy, F. M. Jarvist, M. Frost, M. J. Benjamin and W. Aron, *Phys. Rev. B*, 2019, **99**, 085207.

46 C. Rajneesh, D. Ambesh and P. Ravindra, *Superlattices Microstruct.*, 2018, **122**, 268.

47 Y. Liu, X. Duan, Y. Huang and X. Duan, *Chem. Soc. Rev.*, 2018, **47**, 6388.

48 Y. Xu, Z. Ning, H. Zhang, G. Ni, H. Shao, B. Peng, X. Zhang, X. He, Y. Zhu and H. Zhu, 2017, arXiv preprint arXiv:1701.03715.

49 A. Ramasubramaniam, *Phys. Rev. B: Condens. Matter Mater. Phys.*, 2012, **86**, 115409.

50 B. Wang, J. Nisar and R. Ahuja, *ACS Appl. Mater. Interfaces*, 2012, **4**, 5691.

51 S. Kajita, T. Nakayama and J. Yamauchi, *J. Phys.: Conf. Ser.*, 2006, **29**, 120.

52 N. N. Rosman, R. M. Yunus, L. J. Minggu, K. Arifin, M. N. I. Salehmin, M. A. Mohamed and M. B. Kassim, *Int. J. Hydrogen Energy*, 2018, **43**, 18925.

53 J. Liu, X. L. Fu, S. F. Chen and Y. F. Zhu, *Appl. Phys. Lett.*, 2011, **99**, 191903.

54 H. L. Zhuang and R. G. Hennig, *Phys. Rev. B: Condens. Matter Mater. Phys.*, 2013, **88**, 115314.

55 T. A. Pham, D. Lee, E. Schwegler and G. Galli, *J. Am. Chem. Soc.*, 2014, **136**, 17071.

56 X. Li, J. Yu, J. Low, Y. Fang, J. Xiaoc and X. Chen, *J. Mater. Chem. A*, 2015, **3**, 2485.

This journal is © the Owner Societies 2019

Phys. Chem. Chem. Phys., 2019, **21**, 18612–18621 | 18621